Prominent role of oxygen in the multiferroicity of $DyMnO_3$ and $TbMnO_3$: A resonant soft x-ray scattering spectroscopy study

S. W. Huang,[1,2,3,*] J. M. Lee,[4] Horng-Tay Jeng,[5,6] YuCheng Shao,[7] L. Andrew Wray,[8] J. M. Chen,[4] R. Qiao,[1] W. L. Yang,[1] Y. Cao,[9] J.-Y Lin,[1,10] R. W. Schoenlein,[2,11] and Y.-D. Chuang[1,†]

[1]*Advanced Light Source, Lawrence Berkeley National Laboratory, Berkeley, California 94720, USA*
[2]*Materials Sciences Division, Lawrence Berkeley National Laboratory, Berkeley, California 94720, USA*
[3]*MAX IV Laboratory, Lund University, P. O. Box 118, 221 00 Lund, Sweden*
[4]*National Synchrotron Radiation Research Center, Hsinchu 30076, Taiwan*
[5]*Department of Physics, National Tsing Hua University, Hsinchu 30013, Taiwan*
[6]*Institute of Physics, Academia Sinica, Taipei 11529, Taiwan*
[7]*Department of Physics, Tamkang University, Taipei 25137, Taiwan*
[8]*Department of Physics, New York University, New York, New York 10003, USA*
[9]*Condensed Matter Physics & Materials Sciences Department, Brookhaven National Laboratory, Upton, New York 11973, USA*
[10]*Institute of Physics, National Chiao Tung University, Hsinchu 300, Taiwan*
[11]*Linac Coherent Light Source, SLAC National Accelerator Laboratory, Menlo Park, California 94035, USA*

(Received 27 May 2016; revised manuscript received 6 July 2016; published 21 July 2016)

Oxygen is known to play an important role in the multiferroicity of rare earth manganites; however, how this role changes with rare earth elements is still not fully understood. To address this question, we have used resonant soft x-ray scattering spectroscopy to study the F-type $(0,\tau,0)$ diffraction peak from the antiferromagnetic order in $DyMnO_3$ and $TbMnO_3$. We focus on the measurements at O K edge of these two manganites, supplemented by the results at Mn L_2 and Dy M_5 edge of $DyMnO_3$. We show that the electronic states of different elements are coupled more strongly in $DyMnO_3$ than in $TbMnO_3$, presumably due to the stronger lattice distortion and the tendency to develop E-type antiferromagnetism in the ferroelectric state that promote the orbital hybridization. We also show that the anomaly in the correlation length of $(0,\tau,0)$ peak in $DyMnO_3$ signifies the exchange interaction between Mn and rare earth spins. Our findings reveal the prominent role of oxygen orbitals in the multiferroicity of rare earth manganites and the distinct energetics between them.

DOI: 10.1103/PhysRevB.94.035145

I. INTRODUCTION

Multiferroics are materials in which two or more ferroic orders, such as ferroelasticity, ferroelectricity, and ferromagnetism (or antiferromagnetism), are present simultaneously. When the couplings between these orders are strong, their coexistence offers the advantage to control one order through the perturbations that influence the other electronic degrees of freedom [1–6]. This aspect, in particular using the electric field (charge) and magnetic field (spin) to control ferromagnetism and ferroelectricity, respectively, makes multiferroics extremely useful for electronic technologies because the flexibility in changing the charge and spin states of electrons provides alternative ways to exchange and store digital information [7,8]. However, it is often challenging to find the transition metal oxides that exhibit both strong ferroelectricity and ferromagnetism: the strong Hund's rule coupling tends to enhance ferromagnetism in transition metal ions with a localized, partially filled d shell, whereas covalent bonding to oxygen ligands is important for strong ferroelectricity. In addition, the symmetry requirements for these two ferroic orders are very different.

It is not necessary to have strong ferroic orders for the multiferroics to be useful. Instead, higher degree of tunability and larger response to perturbations are more desirable. Hence an alternative way to discover new multiferroics is through the improper ferroelectric, i.e., ferroelectricity as a parasitic effect of a primary magnetic order, as in the case of orthorhombic manganite $TbMnO_3$ [9] and other $RMnO_3$ and RMn_2O_5 manganites (R = Gd, Tb, and Dy) [10–17]. These rare earth manganites often display a series of magnetic transitions with distinct magnetic orders and electric properties [for example, see Fig. 1(a) for the magnetic and electric properties of $DyMnO_3$]; when they are subjected to the magnetic field or electric field, their responses also vary significantly [18–22].

Several mechanisms, such as antisymmetric inverse Dzyaloshinskii-Moriya (DM) interaction (spin current) [23–25], symmetric Heisenberg exchange interaction (exchange striction) [26–28], spin-dependent Mn-ligand p-d hybridization [29], and other degrees of freedom like orbital and lattice [30–36], have been proposed to contribute to the ferroelectricity in these manganites [4,5]. Although oxygen undoubtedly plays a crucial role in these mechanisms, how this role changes with rare earth elements remains not fully understood. Differences in the role of oxygen are likely to reflect differences in the relative importance of these mechanisms when changing the rare earth elements.

Resonant x-ray scattering spectroscopy is one of the direct probes commonly used to study the electronic orders in correlated materials, and is the ideal technique for elucidating the role of oxygen in these multiferroic manganites [37]. This spectroscopy has been used at rare earth L and M edges and Mn K and L edges, but the studies at O K edge are limited [38–49]. In that regard, we have performed resonant

*shih-wen.huang@maxiv.lu.se
†ychuang@lbl.gov

 ©2016 American Physical Society

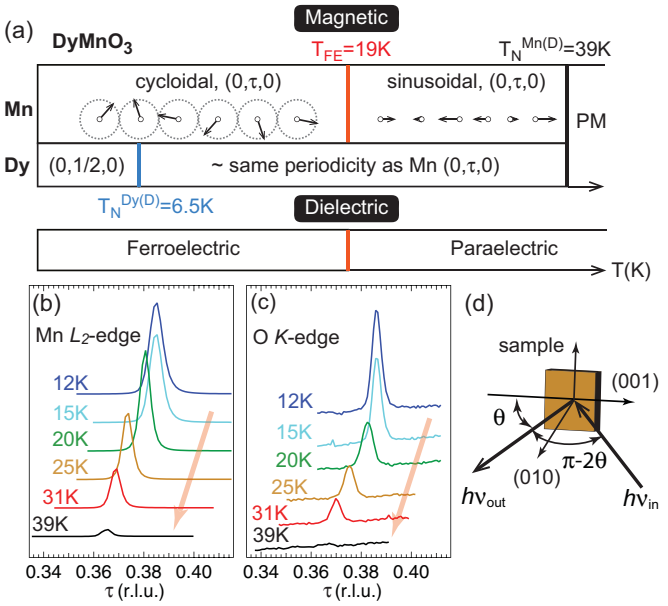

FIG. 1. (a) The schematic plot showing the characteristic temperatures of Mn and Dy spin orders and the electric properties of $DyMnO_3$. (b) and (c) Normalized q scans about the $(0,\tau^{(D)},0)$ wave vector measured at selected temperatures at (b) Mn L_2 edge (645.4 eV) and (c) O K edge (523.75 eV). Spectra are shifted vertically for clarity. (d) The schematic plot showing the experimental setup.

soft x-ray scattering measurements to study the F-type $(0,\tau,0)$ diffraction peak from the antiferromagnetic order in $DyMnO_3$ and $TbMnO_3$. Our results show that the oxygen orbitals are polarized by Mn spin order below 39 K ($DyMnO_3$) or 42 K ($TbMnO_3$). However, the behaviors of oxygen orbitals in these two materials are rather different.

The temperature dependence of wave vector τ and intensity I of $(0,\tau,0)$ diffraction peak measured at O K, Mn L_2, and Dy M_5 edge shows that the electronic states of these elements are coupled more strongly in $DyMnO_3$ than in $TbMnO_3$. The resonance profiles at O K edge in the ferroelectric state exhibit noticeable contribution from the hybridization of oxygen orbitals with localized Mn $4s/4p$ and Dy $6s/6p$ states. However, such hybridization is absent in $TbMnO_3$. Using first-principles calculations, we show that the stronger lattice distortion and the tendency to develop E-type antiferromagnetism in $DyMnO_3$ can contribute to this enhanced orbital hybridization. An anomalous temperature dependence in the correlation length λ of $(0,\tau,0)$ peak can be seen across the ferroelectric transition in $DyMnO_3$. This anomaly, we propose, is caused by the exchange interaction between Mn and rare earth spins in the bc plane. Presence of this exchange interaction and the prominent role played by oxygen orbitals in $DyMnO_3$ signify the energetic differences between these rare earth manganites.

II. EXPERIMENT

Single crystal $DyMnO_3$ and $TbMnO_3$ were grown by flux method, and the details of crystal growth can be found elsewhere [50,51]. All crystals were checked by conventional four-circle diffractometry to confirm the orthorhombically distorted perovskite structure with *Pbnm* space group ($a = 5.28$ Å, $b = 5.84$ Å, $c = 7.38$ Å for $DyMnO_3$ and $a = 5.31$ Å, $b = 5.86$ Å, $c = 7.4$ Å for $TbMnO_3$). For $DyMnO_3$, since the natural growth produced the [1, 1, 0] surface, the [0, 1, 0] and [0, 0, 1] surfaces were aligned in the horizontal scattering plane by mounting the sample on a 45° wedge. For $TbMnO_3$, the single crystal was cut and polished to expose the [0, 1, 0] plane and mounted flat on the sample holder [see Fig. 1(d) for the schematic of experimental setup].

Resonant soft x-ray scattering (RSXS) measurements were carried out at Beamline 8.0.1 at the Advanced Light Source (ALS), Lawrence Berkeley National Laboratory (LBNL), using the RSXS endstation [52]. During the measurements, incident photon polarization was kept in the horizontal scattering plane (π-scattering geometry). The beamline energy resolution was better than 0.3, 0.25, and 0.2 eV at O K (523.75 eV), Mn L_2 (645.4 eV), and Dy M_5 edge (1290 eV), respectively. The beam spot on the sample was around 40 μm (v) by 500 μm (h). All temperature dependence spectra were recorded in the warming process. A photodiode with Al window in the front to block out the ambient light (visible light around the experimental chamber) was used to record the scattered x rays from sample. The angular resolution of this photodiode was 3 mrad, less than 20% of the half-width half-maximum (HWHM) of diffraction peak measured at all edges.

q-scan spectra are presented in this paper. For recording the q scans, incident photon energy was fixed while sample (θ) and detector angles were varied such that the photon momentum transfer was projected along the crystalline $\hat{b}$ axis. The q scans were first normalized by the incident photon flux determined from the photocurrent of an upstream Au mesh, and then fitted with a Lorentzian function on top of a linear background to remove the signals from fluorescence and specular reflection because these two sources only have monotonic $\vec{q}$ dependence. The ordering wave vector τ is determined from the peak centroid. The intensity I is the peak area. The correlation length λ is calculated using the inverse of half-width half-maximum (HWHM) of the Lorentzian peak. The resonance profiles shown in Fig. 3(c) were produced by recording the q scans with incident photon energies varied across the O K edge.

The first-principles calculations were performed using the accurate full-potential augmented-wave method [53,54], as implemented in the VASP package within GGA+U schemes at 0 K. The calculations were performed over the $7 \times 7 \times 5$ ($a \times b \times c$ unit cell) and $7 \times 3 \times 5$ ($a \times 2b \times c$ unit cell) Monkhorst-Pack k-point meshes in the irreducible Brillouin zone for A-type and E-type antiferromagnetism, respectively. Lattice relaxation, which gives lower energy, was also included in the calculations. The on-site Coulomb energy $U = 5.0$ eV and exchange energy $J = 0.87$ eV were used for Mn $3d$ electrons [51].

III. RESULTS AND DISCUSSIONS

Due to multiple absorption edges used in this study to probe specifically the O $2p$, Mn $3d$, and Dy $4f$ electronic states, we adopt the following convention in the discussion: O, Mn, and

Dy in the superscript of τ, I, and λ indicate the measurements at O K, Mn L_2, and Dy M_5 edge, respectively. D and T in ( ) indicate the results from $DyMnO_3$ and $TbMnO_3$.

A. RSXS at O K, Mn L_2, and Dy M_5 edge of $DyMnO_3$

Selected q scans from $DyMnO_3$ at Mn L_2 and O K edge are shown in Figs. 1(b) and 1(c). In $DyMnO_3$, Mn spins form a collinear sinusoidal antiferromagnetic order (AF) along the crystalline $\hat{b}$ axis below $T_N^{Mn(D)}$ ~39 K. When an additional $\hat{c}$-axis component is developed below 19 K, this order becomes a spin spiral [or cycloidal, see Fig. 1(a)]. The antiferromagnetic order produces the first harmonic F-type $(0, \tau^{(D)}, 0)$ diffraction peak that can be measured at Mn L_2 edge [Fig. 1(b)]. When the sample temperature is increased, this $(0, \tau^{Mn(D)}, 0)$ peak becomes weaker and shifts towards a smaller wave vector, consistent with the literature [10,15]. The first new finding of this paper is the observation of a corresponding $(0, \tau^{O(D)}, 0)$ peak at O K edge [Fig. 1(c)]. Compared to $(0, \tau^{Mn(D)}, 0)$, this $(0, \tau^{O(D)}, 0)$ peak displays similar temperature dependence in $I^{O(D)}$ and $\tau^{O(D)}$. Studies on $TbMn_2O_5$ suggested the origin of this peak as the antiferromagnetic ordering of oxygen spins from polarized oxygen orbitals [46]; hence the observation of $(0, \tau^{O(D)}, 0)$ confirms that the oxygen orbitals are indeed involved in the ferroelectricity in $DyMnO_3$.

More information can be obtained from the Lorentzian fitting of these q scans. The temperature dependence of τ, I, and λ of $(0, \tau^{(D)}, 0)$ peak are summarized in Figs. 2(a)–2(e) and Figs. 5(a) and 5(b). Data recorded at O K, Mn L_2, and Dy M_5 edge are represented by black filled circles, blue open circles, and red filled diamonds, respectively. We overlay $\tau^{(D)}$s of different elements in Fig. 2(a) to show the excellent agreement between $\tau^{Mn(D)}$ and $\tau^{O(D)}$, which provides the strong evidence that the polarized oxygen orbitals lock tightly to the Mn spin order below $T_N^{Mn(D)}$. Ordering of Dy spins below $T_N^{Mn(D)}$ was also reported previously and was attributed to the strong coupling between rare earth and Mn spins [38,42,47]. However, $\tau^{Dy(D)}$ does not track $\tau^{Mn(D)}$ as closely as $\tau^{O(D)}$ does. In fact, the difference $\Delta\tau = \tau^{Dy(D)} - \tau^{Mn(D)}$ [right axis, Fig. 2(a)] occurs mainly above the 19 K ferroelectric transition temperature ($T_{FE}^{(D)}$).

Although $I^{O(D)}$ [Fig. 2(b)], $I^{Dy(D)}$ [Fig. 2(d)], and $I^{O(D)}$ [Fig. 2(e)] all exhibit a monotonic decrease with increasing the sample temperature, the rate of decrease $-dI^{(D)}(T)/dT$ shows an abrupt reduction around 20–25 K, just above $T_{FE}^{(D)}$. Such rate change manifests a "kink" in their temperature dependence. One may argue that this kink is the fitting artifact because $\lambda^{(D)}$s also show some changes at similar temperature range and I scales inversely with λ. But this argument does not agree with the decrease in $I^{O(D)}$ [Fig. 2(b)] and $I^{Dy(D)}$ [Fig. 2(d)] around 17 and 20 K when $\lambda^{O(D)}$ [Fig. 2(c)] and $\lambda^{Dy(D)}$ [Fig. 5(b)] decrease concurrently, nor with the behavior seen in $TbMnO_3$ [Figs. 2(h) and 2(i), see later discussion]. The increased peak intensity was previously viewed as an indication of enhanced coupling between Mn and Tb spins [41], and the same notion here would imply the stronger coupling between the electronic states of Mn, Dy, and O in the ferroelectric state.

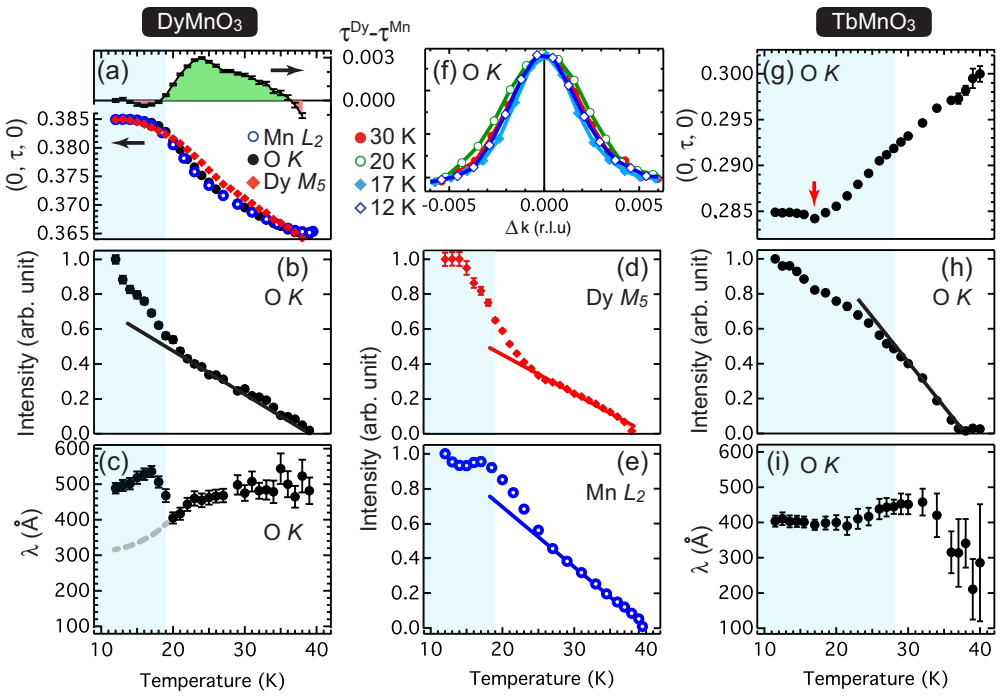

FIG. 2. (a)–(e) Lorentzian fitting results of q scans from $DyMnO_3$ showing the temperature dependence of (a) $\tau^{Mn(D)}$, $\tau^{Dy(D)}$, and $\tau^{O(D)}$, (b) $I^{O(D)}$, (c) $\lambda^{O(D)}$, (d) $I^{Dy(D)}$, and (e) $I^{Mn(D)}$. Black filled circles, blue open circles, and red filled diamonds are data recorded at O K (523.75 eV), Mn L_2 (645.4 eV), and Dy M_5 edge (1290 eV), respectively. The difference in wave vector $\Delta\tau = \tau^{Dy(D)} - \tau^{Mn(D)}$ is shown on top of (a) (right axis). (f) Selected q scans at O K edge. The q scans are scaled in height and shifted in $\vec{k}$ to align the peak centroids for comparison. (g)–(i) Lorentzian fitting results of q scans from $TbMnO_3$ at O K edge (523.75 eV) showing the temperature dependence of (g) $\tau^{O(T)}$, (h) $I^{O(T)}$, and (i) $\lambda^{O(T)}$. Red arrow in (g) marks the lock-in temperature. Light blue regions indicate the ferroelectric state below 19 K $T_{FE}^{(D)}$ (a)–(e) or 28 K $T_{FE}^{(T)}$ (g)–(i). Thin solid lines in (b), (d), (e), and (h) are guides for eyes. The gray dashed line in (c) denotes our conjectured baseline value of $\lambda^{O(D)}$.

What is intriguing in Fig. 2 is the anomaly in the correlation length. $\lambda^{O(D)}$ does not exhibit simple temperature dependence; instead, there is an abrupt decrease around 17 K followed by an increase just above $T_{FE}^{(D)}$ [Fig. 2(c)]. We emphasize that this anomaly is not the fitting artifact either, as it can be clearly seen in the normalized q scans in Fig. 2(f) (the q scans are scaled in height and shifted in $\vec{k}$ to line up the peak centroids for comparison).

B. RSXS at O *K* edge of $TbMnO_3$

RSXS measurements at O K edge were attempted on other multiferroic manganites, like the Tb manganites. In $TbMn_2O_5$, the presence of $(0, \tau^{O(T)}, 0)$ peak was attributed to the presence of antiferromagnetic order of oxygen spins from polarized oxygen orbitals. On the other hand, previous measurements could not find this peak in $TbMnO_3$ [44–46]. Here we repeat the same O K edge measurements on $TbMnO_3$, and unlike previous reports, we have observed this $(0, \tau^{O(T)}, 0)$ peak. The corresponding Lorentzian fitting results are summarized in Figs. 2(g)–2(i).

Comparing the temperature dependence of $\tau^{O(T)}$ in Fig. 2(g) with the $\tau^{(T)}$s in the literature, one immediately notices that contrary to $\tau^{O(D)}$, $\tau^{O(T)}$ does not track the temperature dependence of $\tau^{Mn(T)}$ and $\tau^{Tb(T)}$ at all [41,44,45]. Although the lock-in temperature for $\tau^{Tb(T)}$ is ∼3 K lower than that of $\tau^{Mn(T)}$ at 28 K (ferroelectric transition temperature $T_{FE}^{(T)}$), this temperature for $\tau^{O(T)}$ as marked by the red arrow is even lower: ∼10 K below $T_{FE}^{(T)}$. Besides $\tau^{O(T)}$, $I^{O(T)}$ and $\lambda^{O(T)}$ also show different temperature dependence compared to $I^{O(D)}$ and $\lambda^{O(D)}$: the rate $-dI^{O(T)}(T)/dT$ becomes larger, instead of smaller, above $T_{FE}^{(T)}$ and $I^{O(T)}$ correlates with $\lambda^{O(T)}$ in a different manner. Furthermore, besides a ∼10% increase between 20 and 28 K, $\lambda^{O(T)}$ does not show any cusps like the ones in $\lambda^{O(D)}$. Lastly, there is a clear reduction in $\lambda^{O(T)}$ around $T_N^{Mn(T)}$, which is not seen in $\lambda^{(D)}$s in $DyMnO_3$ [Figs. 2(c), 5(a), and 5(b)].

C. Enhanced oxygen orbital hybridization in $DyMnO_3$

The contrasting temperature dependence in $(0, \tau^{O(D)}, 0)$ [Figs. 2(a)–2(c)] and $(0, \tau^{O(T)}, 0)$ [Figs. 2(g)–2(i)] suggests the different roles played by oxygen orbitals in $DyMnO_3$ and $TbMnO_3$. Results such as the nearly perfect tracking between $\tau^{(D)}$s of different elements relative to $\tau^{(T)}$s, the abrupt decrease in $-dI^{(D)}(T)/dT$ above the ferroelectric transition, and the absence of reduction behavior in $\lambda^{(D)}$s around $T_N^{Mn(D)}$, all imply that the electronic states of different elements are coupled more strongly in $DyMnO_3$ than in $TbMnO_3$ in the ferroelectric state. These findings can be further investigated by looking at the O K edge resonance profiles of $(0,\tau,0)$ peak. The resonance profiles of $(0,\tau^{O(D)},0)$ and $(0,\tau^{O(T)},0)$ peaks measured at 13 K (ferroelectric state) are shown as a red line with filled circles and a blue line with open circles in Fig. 3(c), respectively. For comparison, the x-ray absorption spectrum (XAS) of $DyMnO_3$ recorded in total electron yield mode is shown in Fig. 3(b) and the Mn and Dy spin partial density of states (pDOS) from first-principles calculations are shown in Fig. 3(a) (the Mn and Tb pDOS in $TbMnO_3$ are nearly identical to the Mn and Dy pDOS in $DyMnO_3$, hence they are not shown here) [50,51].

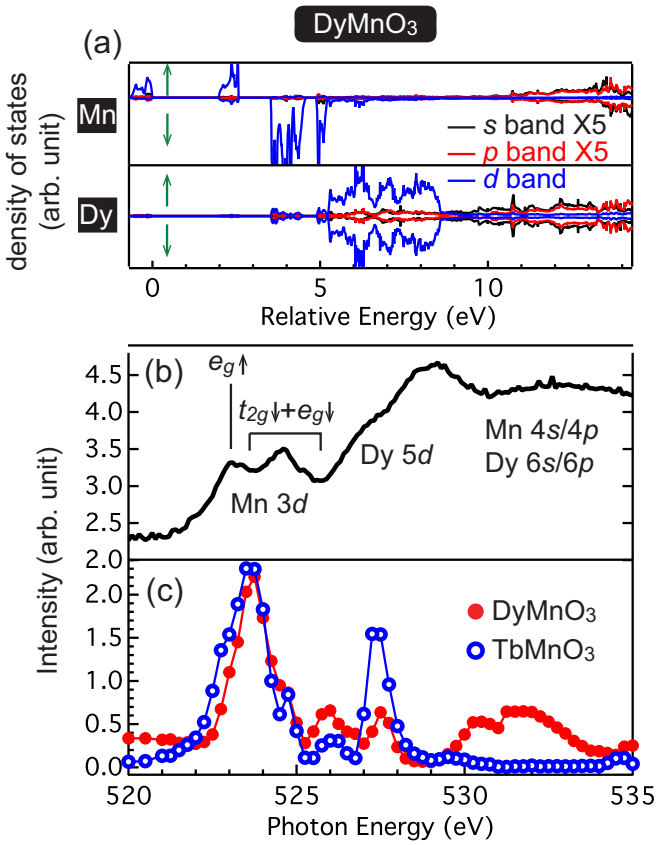

FIG. 3. (a) Mn (top) and Dy (bottom) spin partial density of states (pDOS) from first-principles calculations. The s (black curves) and p bands (red curves) are magnified by a factor of 5 for clarity. (b) X-ray absorption spectrum of $DyMnO_3$ around O K edge recorded in the total electron yield mode at 13 K. The Mn and Dy electronic states that hybridize with oxygen $2p$ orbitals are also labeled in this panel. (c) Resonance profiles of $(0,\tau^{O(D)},0)$ (red line with filled circles) and $(0,\tau^{O(T)},0)$ (blue line with open circles) peaks measured at 13 K.

For clarity, the s (black curves) and p bands (red curves) are magnified by a factor of 5 in this plot.

From Fig. 3(c), one can see that the resonance profiles of these two peaks are very similar in the [522 eV, 526 eV] energy range. Based on Figs. 3(a) and 3(b), this is the energy range for Mn $3d$ $e_{g\uparrow}$ and $t_{2g\downarrow}/e_{g\downarrow}$ states, and seeing strong intensity in the O K edge resonance profiles implies the strong oxygen $2p$ orbital hybridization with Mn $3d$ states. The resonance profiles also display differences in the [526 eV, 529 eV] energy range, suggesting that the oxygen orbitals hybridize differently with different rare earth $5d$ states. However, what is surprising in this figure is the presence of a broad hump in the resonance profile of $(0,\tau^{O(D)},0)$ peak in the [530 eV, 535 eV] energy range only. This [530 eV, 535 eV] energy range corresponds to the high energy Mn $4s/4p$ and Dy $6s/6p$ states, as determined from Fig. 3(a). The presence of this broad hump signifies the finite oxygen orbital hybridization with Mn $4s/4p$ and rare earth $6s/6p$ states in $DyMnO_3$, but not in $TbMnO_3$.

Oxygen orbitals can hybridize with other electronic states near the Fermi energy, such as Mn $3d$ states in this case. Therefore, seeing finite intensity in the resonance profiles of $(0, \tau^{O(D,T)}, 0)$ peak between 522 and 526 eV is not

unexpected. In fact, similar phenomenon has been reported in transition metal oxides where the ordering of transition metal electronic states has strong oxygen character (for example, see [55]). However, seeing hybridization with higher energy Mn/Dy s and p states is surprising because this calls for mechanisms that involve higher energy scales. It is known that the size of rare earth ions decreases when going from La to Ho; consequently, the lattice distortion is enhanced through tilting and deformation of MnO_6 octahedral. The enhanced lattice distortion changes the relative strength of spin interactions and the magnetic ground state evolves from A-type ($LaMnO_3$) to collinear sinusoidal ($Tb/DyMnO_3$) to E-type antiferromagnetism ($HoMnO_3$) [10,12]. In addition, the tendency for orbital mixing and orbital ordering becomes stronger [56–58]. With $DyMnO_3$ experiencing stronger lattice distortion than $TbMnO_3$, we believe that the oxygen orbitals in $DyMnO_3$ can further encroach upon the high energy, localized Mn/Dy s and p states to promote the hybridization.

Besides looking from the lattice point of view, it was recently pointed out that the polarization of oxygen orbitals can also contribute to the ferroelectricity, as in the case of $HoMnO_3$ [31]. This mechanism was realized from the asymmetry in the in-plane Mn-O bond lengths and a higher degree of delocalization for oxygen orbitals with E-type antiferromagnetism, together these factors give rise to the directional dependence in the Mn-O orbital hybridization. To elaborate on this point, we show the iso-charge surface of $DyMnO_3$ from first-principles calculations in Fig. 4. In the DFT calculations, we implemented the A-type [Figs. 4(a), 4(c), 4(e), and 4(f)] and E-type antiferromagnetism [Figs. 4(b), 4(d), 4(g), and 4(h)] that do not naturally occur in $DyMnO_3$. These two magnetic states are schematically illustrated by color arrows in Figs. 4(a) and 4(b). The calculated pDOS is then summed over two spin flavors and integrated over [−0.74 eV, 0 eV] energy window to generate the iso-charge surface. With relaxed crystal structures, the E-type antiferromagnetism clearly shows four inequivalent in-plane Mn-O bonds, whereas A-type antiferromagnetism only shows two pairs of inequivalent Mn-O bonds (the difference in the bond length is also listed in Table I). From the iso-charge surface plots, it is clear that in addition to the enhanced lattice distortion, E-type antiferromagnetism also exhibits more delocalized orbitals at both Mn and O sites [Figs. 4(b) and 4(d)], in agreement with previous results [31].

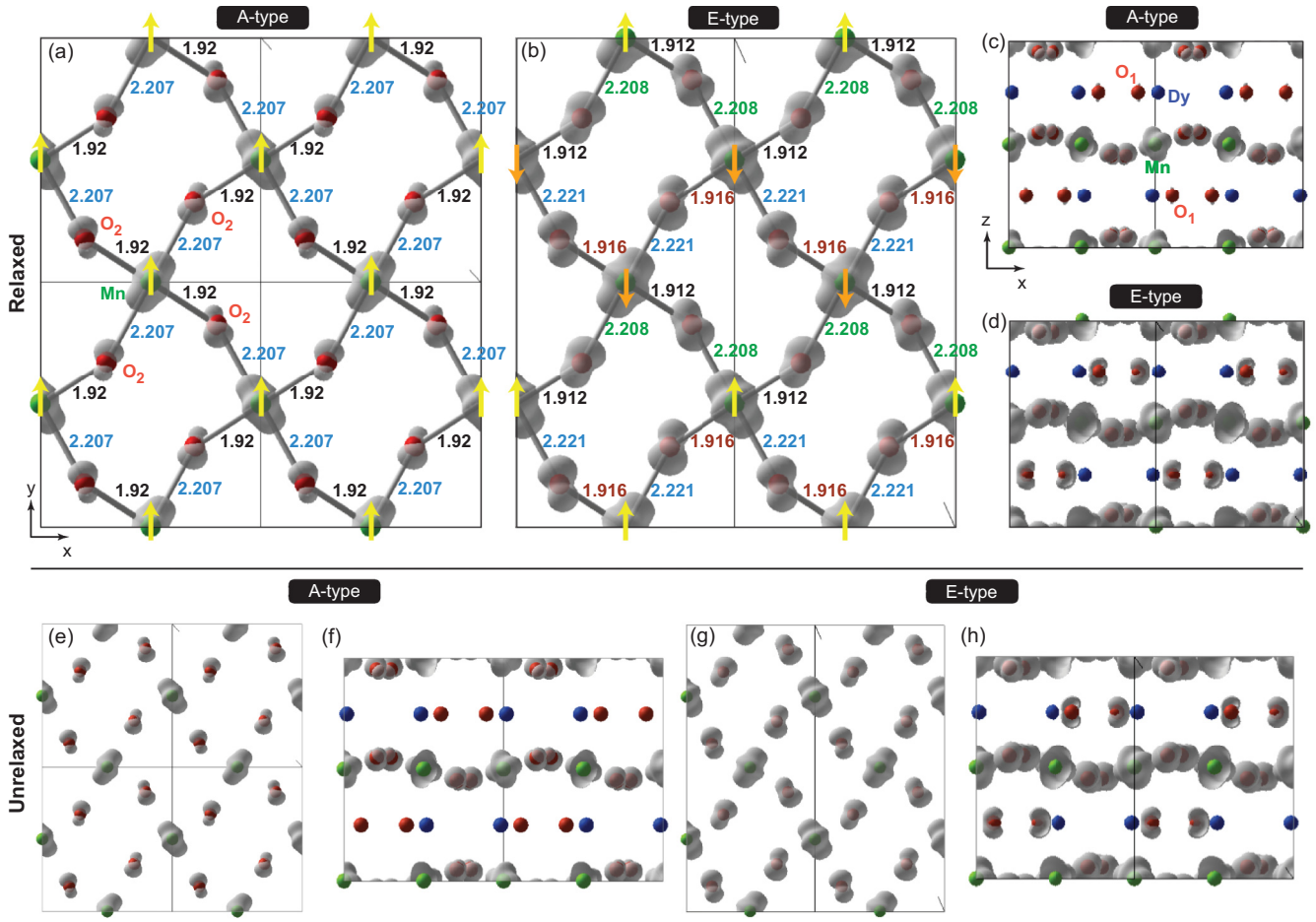

FIG. 4. Iso-charge surface of $DyMnO_3$ with (a) and (c) A-type and (b) and (d) E-type antiferromagnetism using relaxed crystal structures. The in-plane and out-of-plane results are shown in (a) and (b) and (c) and (d), respectively. The iso-charge surface is produced by integrating the DFT density of states (summed over spins) over [−0.74 eV, 0 eV] energy window. The magnetic orders are illustrated by the color arrows. The calculated Mn-O bond lengths are listed in (a) and (b), and also summarized in Table I. (e)–(h) Iso-charge surface of $DyMnO_3$ with (e) and (f) A-type and (g) and (h) E-type antiferromagnetism without relaxing the crystal structures (frozen structure). The Mn-O bond lengths are also summarized in Table I. O_1 and O_2 denote the out-of-plane and in-plane oxygens, respectively.

TABLE I. Mn-O bond length of $DyMnO_3$ from first-principles calculations

	Mn-O_1(1) (Å)	Mn-O_1(2) (Å)	Mn-O_2(1) (Å)	Mn-O_2(2) (Å)	Mn-O_2(3) (Å)	Mn-O_2(4) (Å)
A-/E-AF, unrelaxed	1.938	1.938	1.883	1.883	2.24	2.24
A-AF relaxed	1.957 (0.019)[a]	1.957 (0.019)	1.92 (0.037)	1.92 (0.037)	2.207 (−0.033)	2.207 (−0.033)
E-AF relaxed	1.953 (0.015)	1.954 (0.016)	1.912 (0.029)	1.916 (0.033)	2.208 (−0.032)	2.221 (−0.019)

[a]( ) is the difference between relaxed and unrelaxed bond lengths.

Surprisingly, this orbital delocalization can even be induced by the magnetic interactions only. We repeat the same calculations with frozen (unrelaxed) structure, e.g., same lattice parameters from the Inorganic Crystal Structure Database (ICSD) for A-type and E-type antiferromagnetism, and the resulting iso-charge surfaces are shown in Figs. 4(e)–4(h). From these figures, one can see that even with frozen structure, the degree of orbital delocalization is still much higher with E-type antiferromagnetism than with A-type antiferromagnetism. With $\tau^{(D)}$s of different elements approaching the $(H,K,L) = (0,1/2,0)$ E-type antiferromagnetic ordering wave vector in the ferroelectric state while $\tau^{(T)}$s moving away from it, we speculate that the degree of delocalization for oxygen orbitals will become even higher in $DyMnO_3$. In this scenario, the observed hybridization between oxygen orbitals and Mn $4s/4p$ and Dy $6s/6p$ states in Fig. 3(c) can also be related to their disparate magnetic interactions.

D. Coupling between Mn and Dy spins below $T_{FE}^{(D)}$

The distinct energetics of $DyMnO_3$ and $TbMnO_3$ are also manifested in other exchange interactions. In Figs. 5(a) and 5(b) we show the temperature dependence of $\lambda^{Mn(D)}$ and $\lambda^{Dy(D)}$. $\lambda^{Dy(D)}$ is consistently shorter than $\lambda^{Mn(D)}$ and $\lambda^{O(D)}$, which may be related to the induced nature of Dy spin order above its 6.5 K commensurate ordering temperature [Fig. 1(a)]. $\lambda^{Mn(D)}$ and $\lambda^{Dy(D)}$ both exhibit ∼20%–25% increase from low temperatures to above $T_{FE}^{(D)}$, suggesting that the Mn and Dy spin ordered domains actually expand when transitioning from low temperature bc-plane spin spiral phase to high temperature collinear sinusoidal antiferromagnetic phase. Even without fitting, changes in the correlation length can already be seen in the normalized q scans at Mn L_2 edge [Fig. 5(c), q scans at Dy M_5 edge are not shown here]. Although one can argue that such increase in correlation length can also be seen in $\lambda^{O(T)}$ around $T_{FE}^{(T)}$, which can be related to the change in optical properties that leads to a longer x-ray probe depth at high temperature (hence longer correlation length), the magnitude of increase in $\lambda^{Mn(D)}$ and $\lambda^{Dy(D)}$ is too large (by about a factor of 2) to be explained by this cause, let alone the cusps in the temperature dependence of $\lambda^{O(D)}$. Shorter $\lambda^{Mn(D)}$ and $\lambda^{Dy(D)}$ below $T_{FE}^{(D)}$ may seem to contradict the behaviors in $I^{(D)}$s of different elements and the general belief that rare earth (Tb and Dy) and Mn spins are coupled more strongly in the ferroelectric state [41,42,44,45], but we will show that this is the manifestation of an exchange coupling between Mn and Dy spins that is further amplified by the perfect locking between $\tau^{(D)}$s.

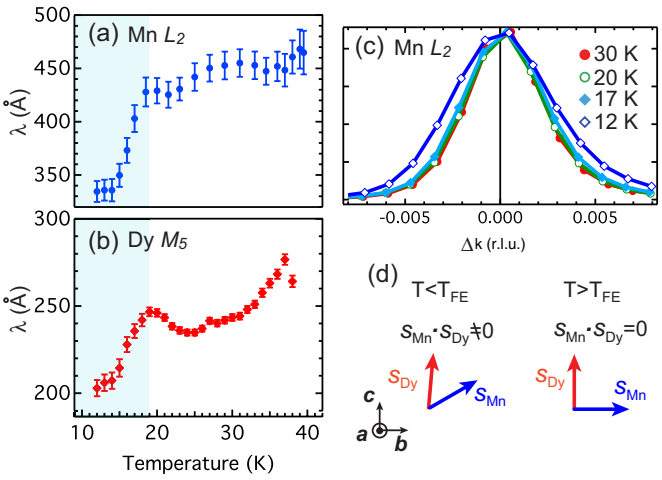

FIG. 5. Lorentzian fitting results of q scans from $DyMnO_3$ showing the temperature dependence of (a) $\lambda^{Mn(D)}$ and (b) $\lambda^{Dy(D)}$. (c) Selected q scans at Mn L_2 edge. (d) The schematic plot illustrating the symmetric exchange coupling H_{df} between Dy (red arrows) and Mn (blue arrows) spins below (left panel) and above $T_{FE}^{(D)}$ (right panel).

The results in Figs. 5(a) and 5(b) can be understood by looking at the relative arrangement of Dy (red arrows) and Mn spins (blue arrows) below $T_N^{Mn(D)}$, as schematically illustrated in Fig. 5(d). For $DyMnO_3$, above $T_{FE}^{(D)}$, Mn and Dy spins are pointing along the crystalline $\hat{b}$ and $\hat{c}$ axis, respectively. They develop canted orientations below $T_{FE}^{(D)}$, giving rise to the spin spiral structures [21,38,42,47]. Spin exchange interactions, whether symmetric Heisenberg or antisymmetric inverse Dzyaloshinskii-Moriya (DM) interactions, have been extensively discussed in the literature. However, most previous discussions focused on the interactions between Mn spins and few did on the interactions with rare earth spins, despite they are strongly coupled even below $T_N^{Mn(D,T)}$ [38,39]. Here the large rare earth $4f$ moment acting as an internal Zeeman field ($\vec{H}_{in}$) can influence the Mn spins ($\vec{s}$) through the Hamiltonian $H_{df} = g\mu_B \Sigma_i \vec{s}_i \cdot \vec{H}_{in}$ [28]. For $DyMnO_3$, H_{df} is 0 above $T_{FE}^{(D)}$ and finite below $T_{FE}^{(D)}$ when Mn and Dy spins are no longer perpendicular to each other [Fig. 5(d)]. Enhanced by the perfect locking between $\tau^{Mn(D)}$ and $\tau^{Dy(D)}$ below $T_{FE}^{(D)}$ [Fig. 2(a)], this Hamiltonian can disrupt the bc-plane spin spirals, leading to the smaller ordered domains. This H_{df} may also be responsible for the strong hysteresis effect in $DyMnO_3$ [59]. Although the H_{df} may affect the Tb and Mn spins in $TbMnO_3$ as the Tb spin also exhibits a finite component along the $\hat{b}$ axis in the ferroelectric phase, the effect can be different due to the disparate tracking behavior in the $\tau^{(T)}$s [60–62]. Further examination on the behavior of $\lambda^{Tb(T)}$ and $\lambda^{Mn(T)}$ may provide valuable insight to this subject.

Comparing the temperature dependence of $\lambda^{(D)}$s, one can see that the increase in $\lambda^{(D)}$s when raising the sample

temperature takes place just below the ferroelectric transition. However, $\lambda^{O(D)}$ displays the puzzling zigzag behavior that is not see in $\lambda^{Mn(D)}$ and $\lambda^{Dy(D)}$. As discussed earlier, the increase in correlation lengths can be attributed to the suppression of competition between H_{df} and presumably the inverse Dzyaloshinskii-Moriya interaction that stabilizes the bc-plane spin spiral below $T_{FE}^{(D)}$. Then this zigzag behavior in $\lambda^{O(D)}$ can be viewed as an outcome of an additional contribution below 17 K, which we suggest comes from the enhanced hybridization between oxygen orbitals and the Mn/Dy electronic states, on top of a baseline value denoted by the gray dashed line in Fig. 2(c).

IV. CONCLUSIONS

We have used RSXS spectroscopy to study the multiferroic $DyMnO_3$ and $TbMnO_3$ and have observed the F-type $(0,\tau,0)$ diffraction peak at O K edge in both materials. The temperature dependence of this diffraction peak shows that the electronic states of different elements are coupled more strongly in $DyMnO_3$ than in $TbMnO_3$. With first-principles calculations, we suggest that the stronger latticed distortion and the tendency to develop E-type antiferromagnetism in $DyMnO_3$ can contribute to the enhanced orbital hybridization in the ferroelectric state. The anomaly in the correlation lengths around the ferroelectric transition in $DyMnO_3$ is explained as the manifestation of competition between the exchange interaction H_{df} and presumably the inverse Dzyaloshinskii-Moriya interaction. With enhanced orbital hybridization in the ferroelectric state that can help restore the antiferromagnetic order in the oxygen orbitals, $\lambda^{O(D)}$ displays the zigzag temperature dependence around $T_{FE}^{(D)}$. The contrasting temperature dependence between $(0, \tau^{O(D)}, 0)$ and $(0, \tau^{O(T)}, 0)$, as well as the presence of H_{df} in $DyMnO_3$, highlight the complex nature of multiferroicity in these manganites, and we propose that mechanisms based on electronic correlations can be more influential to the multiferroicity in manganites with smaller rare earth elements.

ACKNOWLEDGMENTS

This research was supported by the U.S. Department of Energy, Office of Science, Office of Basic Energy Sciences (BES) under Contract No. DE-AC02-05CH11231 (LBNL), and used resources of the Advanced Light Source which is a DOE Office of Science User Facility at LBNL. S.W.H and R.W.S acknowledge support from the Ultrafast Materials Program at LBNL. J.Y.L. is supported by the MOST of Taiwan, R.O.C. under Grant 103-2112-M-009-007-MY3 and the MOE ATU program.

S.W.H. and J.M.L. contributed equally to this work.

[1] N. A. Spaldin and M. Fiebig, Science **309**, 391 (2005).
[2] S. W. Cheong and M. Mostovoy, Nat. Mater. **6**, 13 (2007).
[3] T. Kimura, Annu. Rev. Mater. Res. **37**, 387 (2007).
[4] Y. Tokura and S. Seki, Adv. Mater. **22**, 1554 (2010).
[5] Y. Tokura, S. Seki, and N. Nagaosa, Rep. Prog. Phys. **77**, 076501 (2014).
[6] Y. Yamasaki, H. Sagayama, T. Goto, M. Matsuura, K. Hirota, T. Arima, and Y. Tokura, Phys. Rev. Lett. **98**, 147204 (2007).
[7] W. Eerenstein, N. D. Mathur, and J. F. Scott, Nature (London) **442**, 759 (2006).
[8] J. F. Scott, Science **315**, 954 (2007).
[9] T. Kimura, T. Goto, H. Shintani, K. Ishizaka, T. Arima, and Y. Tokura, Nature (London) **426**, 55 (2003).
[10] T. Kimura, S. Ishihara, H. Shintani, T. Arima, K. T. Takahashi, K. Ishizaka, and Y. Tokura, Phys. Rev. B **68**, 060403 (2003).
[11] N. Hur, S. Park, P. A. Sharma, J. S. Ahn, S. Guha, and S.-W. Cheong, Nature (London) **429**, 392 (2004).
[12] T. Goto, T. Kimura, G. Lawes, A. P. Ramirez, and Y. Tokura, Phys. Rev. Lett. **92**, 257201 (2004).
[13] T. Kimura, G. Lawes, T. Goto, Y. Tokura, and A. P. Ramirez, Phys. Rev. B **71**, 224425 (2005).
[14] M. Kenzelmann, A. B. Harris, S. Jonas, C. Broholm, J. Schefer, S. B. Kim, C. L. Zhang, S.-W. Cheong, O. P. Vajk, and J. W. Lynn, Phys. Rev. Lett. **95**, 087206 (2005).
[15] R. Feyerherm, E. Dudzik, N. Aliouane, and D. N. Argyriou, Phys. Rev. B **73**, 180401(R) (2006).
[16] T. Arima, T. Goto, Y. Yamasaki, S. Miyasaka, K. Ishii, M. Tsubota, T. Inami, Y. Murakami, and Y. Tokura, Phys. Rev. B **72**, 100102(R) (2005).
[17] T. Arima, A. Tokunaga, T. Goto, H. Kimura, Y. Noda, and Y. Tokura, Phys. Rev. Lett. **96**, 097202 (2006).
[18] N. Aliouane, D. N. Argyriou, J. Strempfer, I. Zegkinoglou, S. Landsgesell, and M. v. Zimmermann, Phys. Rev. B **73**, 020102(R) (2006).
[19] D. N. Argyriou, N. Aliouane, J. Strempfer, I. Zegkinoglou, B. Bohnenbuck, K. Habicht, and M. v. Zimmermann, Phys. Rev. B **75**, 020101(R) (2007).
[20] J. Strempfer, B. Bohnenbuck, M. Mostovoy, N. Aliouane, D. N. Argyriou, F. Schrettle, J. Hemberger, A. Krimmel, and M. v. Zimmermann, Phys. Rev. B **75**, 212402 (2007).
[21] R. Feyerherm, E. Dudzik, A. U. B. Wolter, S. Valencia, O. Prokhnenko, A. Maljuk, S. Landsgesell, N. Aliouane, L. Bouchenoire, S. Brown, and D. N. Argyriou, Phys. Rev. B **79**, 134426 (2009).
[22] T. Aoyama, A. Iyama, K. Shimizu, and T. Kimura, Phys. Rev. B. **91**, 081107(R) (2015).
[23] H. Katsura, N. Nagaosa, and A. V. Balatsky, Phys. Rev. Lett. **95**, 057205 (2005).
[24] M. Mostovoy, Phys. Rev. Lett. **96**, 067601 (2006).
[25] I. A. Sergienko and E. Dagotto, Phys. Rev. B **73**, 094434 (2006).
[26] M. Mochizuki and N. Furukawa, Phys. Rev. B **80**, 134416 (2009).
[27] M. Mochizuki, N. Furukawa, and N. Nagaosa, Phys. Rev. Lett. **105**, 037205 (2010).
[28] M. Mochizuki and N. Furukawa, Phys. Rev. Lett. **105**, 187601 (2010).
[29] C. Jia, S. Onoda, N. Nagaosa, and J. H. Han, Phys. Rev. B **76**, 144424 (2007).

[30] D. Efremov, J. van den Brink, and D. Khomskii, Nat. Mater. **3**, 853 (2004).
[31] S. Picozzi, K. Yamauchi, B. Sanyal, I. A. Sergienko, and E. Dagotto, Phys. Rev. Lett. **99**, 227201 (2007).
[32] J. J. Betouras, G. Giovannetti, and J. van den Brink, Phys. Rev. Lett. **98**, 257602 (2007).
[33] S. Dong, R. Yu, J.-M. Liu, and E. Dagotto, Phys. Rev. Lett. **103**, 107204 (2009).
[34] B. H. Kim and B. I. Min, Phys. Rev. B **80**, 064416 (2009).
[35] J. L. Ribeiro and L. G. Vieira, Phys. Rev. B **82**, 064410 (2010).
[36] M. Schiebl, A. Shuvaev, A. Pimenov, G. E. Johnstone, V. Dziom, A. A. Mukhin, V. Yu. Ivanov, and A. Pimenov, Phys. Rev. B **91**, 224205 (2015).
[37] S. W. Lovesey and S. P. Collins, *X-Ray Scattering and Absorption by Magnetic Materials, Oxford Series on Synchrotron Radiation* (Clarendon, Oxford, 1996).
[38] O. Prokhnenko, R. Feyerherm, E. Dudzik, S. Landsgesell, N. Aliouane, L. C. Chapon, and D. N. Argyriou, Phys. Rev. Lett. **98**, 057206 (2007).
[39] O. Prokhnenko, R. Feyerherm, M. Mostovoy, N. Aliouane, E. Dudzik, A. U. B. Wolter, A. Maljuk, and D. N. Argyriou, Phys. Rev. Lett. **99**, 177206 (2007).
[40] J. Strempfer, B. Bohnenbuck, I. Zegkinoglou, N. Aliouane, S. Landsgesell, M. v. Zimmermann, and D. N. Argyriou, Phys. Rev. B **78**, 024429 (2008).
[41] J. Voigt, J. Persson, J. W. Kim, G. Bihlmayer, and Th. Brückel, Phys. Rev. B **76**, 104431 (2007).
[42] N. Aliouane, O. Prokhnenko, R. Feyerherm, M. Mostovoy, J. Strempfer, K. Habicht, K. C. Rule, E. Dudzik, A. U. B. Wolter, A. Maljuk, and D. N. Argyriou, J. Phys: Condens. Matter **20**, 434215 (2008).
[43] R. A. Ewings, A. T. Boothroyd, D. F. McMorrow, D. Mannix, H. C. Walker, and B. M. R. Wanklyn, Phys. Rev. B **77**, 104415 (2008).
[44] T. R. Forrest, S. R. Bland, S. B. Wilkins, H. C. Walker, T. A. W. Beale, P. D. Hatton, D. Prabhakaran, A. T. Boothroyd, D. Mannix, F. Yakhou, and D. F. McMorrow, J. Phys: Condens. Matter **20**, 422205 (2008).
[45] S. B. Wilkins, T. R. Forrest, T. A. W. Beale, S. R. Bland, H. C. Walker, D. Mannix, F. Yakhou, D. Prabhakaran, A. T. Boothroyd, J. P. Hill, P. D. Hatton, and D. F. McMorrow, Phys. Rev. Lett. **103**, 207602 (2009).
[46] T. A. W. Beale, S. B. Wilkins, R. D. Johnson, S. R. Bland, Y. Joly, T. R. Forrest, D. F. McMorrow, F. Yakhou, D. Prabhakaran, A. T. Boothroyd, and P. D. Hatton, Phys. Rev. Lett. **105**, 087203 (2010).
[47] E. Schierle, V. Soltwisch, D. Schmitz, R. Feyerherm, A. Maljuk, F. Yokaichiya, D. N. Argyriou, and E. Weschke, Phys. Rev. Lett. **105**, 167207 (2010).
[48] U. Staub, Y. Bodenthin, M. García-Fernández, R. A. de Souza, M. Garganourakis, E. I. Golovenchits, V. A. Sanina, and S. G. Luschnikov, Phys. Rev. B **81**, 144401 (2010).
[49] S. Partzsch, S. B. Wilkins, E. Schierle, J. E. Hamann-Borrero, H. Wadati, V. Soltwisch, J. P. Hill, E. Weschke, D. Souptel, B. Büchner, and J. Geck, Eur. Phys. J. Special Topics **208**, 133 (2012).
[50] J. M. Chen, C. K. Chen, T. L. Chou, I. Jarrige, H. Ishii, K. T. Lu, Y. Q. Cai, K. S. Liang, J. M. Lee, S. W. Huang, T. J. Yang, C. C. Shen, R. S. Liu, J. Y. Lin, H. T. Jeng, and C.-C. Kao, Appl. Phys. Lett. **91**, 054108 (2007).
[51] J. M. Chen, Z. Hu, H. T. Jeng, Y. Y. Chin, J. M. Lee, S. W. Huang, K. T. Lu, C. K. Chen, S. C. Haw, T. L. Chou, H.-J. Lin, C. C. Shen, R. S. Liu, A. Tanaka, L. H. Tjeng, and C. T. Chen, Phys. Rev. B **81**, 201102(R) (2010).
[52] D. Doering, Y.-D. Chuang, N. Andresen, K. Chow, D. Contarato, C. Cummings, E. Domning, J. Joseph, J. S. Pepper, B. Smith, G. Zizka, C. Ford, W. S. Lee, M. Weaver, L. Patthey, J. Weizeorick, Z. Hussain, and P. Denes, Rev. Sci. Instrum. **82**, 073303 (2011).
[53] P. E. Blöchl, Phys. Rev. B **50**, 17953 (1994).
[54] G. Kresse and D. Joubert, Phys. Rev. B **59**, 1758 (1999).
[55] P. Abbamonte, A. Rusydi, S. Smadici, G. D. Gu, G. A. Sawatzky, and D. L. Feng, Nat. Phys. **1**, 155 (2005).
[56] G. Maris, V. Volotchaev, and T. T. M. Palstra, New J. Phys. **6**, 153 (2004).
[57] M. W. Kim, S. J. Moon, J. H. Jung, J. Yu, S. Parashar, P. Murugavel, J. H. Lee, and T. W. Noh, Phys. Rev. Lett. **96**, 247205 (2006).
[58] F.-K. Chiang, M.-W. Chu, F. C. Chou, H. T. Jeng, H. S. Sheu, F. R. Chen, and C. H. Chen, Phys. Rev. B **83**, 245105 (2011).
[59] T. Finger, K. Binder, Y. Sidis, A. Maljuk, D. N. Argyriou, and M. Braden, Phys. Rev. B **90**, 224418 (2014).
[60] D. Mannix, D. F. McMorrow, R. A. Ewings, A. T. Boothroyd, D. Prabhakaran, Y. Joly, B. Janousova, C. Mazzoli, L. Paolasini, and S. B. Wilkins, Phys. Rev. B **76**, 184420 (2007).
[61] F. Fabrizi, H. C. Walker, L. Paolasini, F. de Bergevin, A. T. Boothroyd, D. Prabhakaran, and D. F. McMorrow, Phys. Rev. Lett. **102**, 237205 (2009).
[62] H. C. Walker, F. Fabrizi, L. Paolasini, F. de Bergevin, J. Herrero-Martin, A. T. Boothroyd, D. Prabhakaran, and D. F. McMorrow, Science **333**, 1273 (2011).